Reconstruction of multidimensional nonlinear polarization response of Pancharatnam-Berry metasurfaces

Zhanjie Gao,[1] Patrice Genevet,[2] Guixin Li,[3] and Konstantin E. Dorfman[1,*]

[1]*State Key Laboratory of Precision Spectroscopy, East China Normal University, Shanghai 200062, China*

[2]*Université Côte d'Azur, CNRS, CRHEA, rue Bernard Gregory, 06560 Valbonne, France*

[3]*Department of Materials Science and Engineering, Shenzhen Institute for Quantum Science and Engineering, Southern University of Science and Technology, Shenzhen 518055, China*

(Received 20 March 2021; revised 11 July 2021; accepted 14 July 2021; published 19 August 2021)

Pancharatnam-Berry (PB) metasurfaces have been considered as innovative optical devices for efficient manipulation of both the phase and the polarization of the electromagnetic field. Here, we present the simultaneous generation of circularly, elliptically, and linearly polarized states by the simplest PB metasurface with one-dimensional phase gradient unit cells. Furthermore, we propose that the reconstruction of a multidimensional nonlinear polarization response of a nanomaterial can be achieved in a single heterodyne measurement by active manipulation of the polarization states of incident light. Using multidimensional spectroscopy, we demonstrate the possibility to track both stationary and transient delocalized charge distributions via detecting plasmonic populations and coherences.

DOI: 10.1103/PhysRevB.104.054303

I. INTRODUCTION

The polarization control of fundamental waves is essential for analyzing different contributions to the nonlinear response. For instance, measurements of molecular orientation and chirality [1,2], the distinguishing of the dipoles and higher multipoles of nanoparticles [3,4], and the polarization-resolved imaging of multiple scattering [5] are all based on the polarization control of the nonlinear response. Currently, Pancharatnam-Berry (PB) metasurfaces, composed of anisotropic meta-atoms with periodic rotating orientations in a two-dimensional plane, allow a simultaneous multichannel generation of different polarization states by designing the local orientation of the meta-atoms [6–14]. More importantly, various nonlinear signals, such as second-harmonic [15–17], third-harmonic [18–20], and four-wave-mixing [21,22] signals in metasurfaces, exhibit enhancement of nonlinear response, wave-front control, vortex beam generation, holography, and encryption.

The constructive and destructive interferences between different susceptibility components control the polarization conversion efficiency of each channel of a PB metasurface [23–26]. This feature provides the possibility of designing PB metasurfaces capable of overcoming the constraints of conventionally multiple polarization-dependent measurements for identifying individual contributions to the nonlinear response [27–29]. However, several main challenges hinder the applicability of the PB metasurface. Firstly, to exhibit multiple polarization responses in a single setup, sufficient transmission channels corresponding to different linear combinations of the same set of susceptibility components are required. The multichannel polarization control of the PB metasurface strongly depends on the geometric phase (PB phase) induced by the rotation of identical birefringent meta-atoms. Therefore the existing linear response techniques require complex metasurface unit cell geometry or near-field couplings among adjacent meta-atoms to exhibit multiple-channel transmission [30–32]. Secondly, while the PB metasurface has been used to manipulate the nonlinear response, such as monolayers of transition metal dichalcogenides [33,34], the full material-specific polarization control and the corresponding microscopic information that contains electronic and plasmonic properties, such as plasmonic coherences and the electronic structure of the metasurfaces, have not been investigated.

In this paper, we show a general approach for reconstruction of the far-field polarization-dependent third-order nonlinear response using a PB metasurface. We develop an analytical formalism that provides qualitative understanding of the physical mechanisms of PB-phase-based control of polarization and the wave front with incoming waves with arbitrary polarization. We first show that a PB metasurface composed of simple one-dimensional (1D) unit cells of nanoantennas simultaneously provides five different polarization conversion and transmission channels in a single measurement for a single linearly polarized (LP) incident beam. Our theory provides a concise and intuitive analytical description that reveals all components of the polarization-dependent third-order susceptibility tensor elements for each scattering order. Secondly, by carefully choosing the polarization configurations of the incident light beams, the signal composition of each scattering channel can be measured independently from the other scattering channels and used to distinguish the different contributions to the total third-order nonlinear response. As an example, we calculate the four-wave-mixing response

*dorfmank@lps.ecnu.edu.cn

 ©2021 American Physical Society

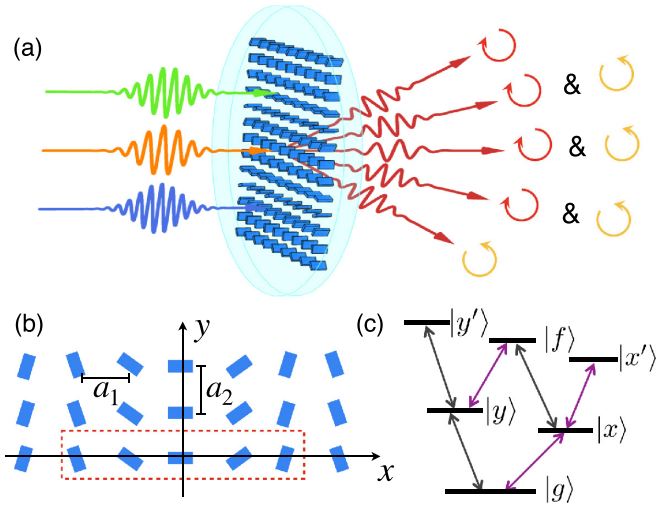

FIG. 1. (a) Sketch of the generation of the third-order nonlinear response giving rise to five beams for a single four-wave-mixing process in a nonlinear PB metasurface. The arrowed circles represent the direction of the circular polarization state of each beam. (b) Schematic of the metasurface. The length and width of the antenna are l_x and l_y, respectively. The distance between two antennas along the x and y axes is a_1 and a_2, respectively. Every nanopillar along the x axis is rotated by $\frac{\pi}{5}$ relative to its neighbor. For the third-order nonlinear process, the unit cell of the periodic structure is depicted by the red dashed box and includes $M = 5$ nanopillars. (c) Six-level system with $\omega_x = 460$ THz, $\omega_y = 500$ THz, $\omega_f = 1075$ THz, $\omega_{x'} = 989$ THz, $\omega_{y'} = 1125$ THz, $\mu_y = 0.6\mu_x$, decay $\gamma = 10$ THz.

as a function of three incoming frequencies and one signal frequency. Utilizing the instruments of multidimensional spectroscopy [35], we extract the susceptibility components as a function of one incoming and one detected frequency, which reveals both stationary as well as transient delocalized charge density via plasmonic population (occupation) and coherence [36] components.

II. MESOSCOPIC MODEL FOR A NONLINEAR PB METASURFACE

As shown in Fig. 1, three plane waves shines on the PB metasurface made of a structure of 1D superlattice corresponding to the lattice primitive translation $\boldsymbol{\varrho}_{m,n} = m\boldsymbol{M}\boldsymbol{a}_1 + n\boldsymbol{a}_2$ and the reciprocal lattice $\boldsymbol{G}_{mn} = \frac{2\pi m}{Ma_1}\boldsymbol{e}_x + \frac{2\pi n}{a_2}\boldsymbol{e}_y$, with vectors $\boldsymbol{a}_1 = a_1\boldsymbol{e}_x$, $\boldsymbol{a}_2 = a_2\boldsymbol{e}_y$.

The classical formulation of the wave scattering problem is based on the set of Maxwell equations without external currents and charges (cgs units) [37,38]

$$\nabla \cdot \boldsymbol{D} = 0, \tag{1}$$

$$\nabla \times \boldsymbol{E} = -\frac{1}{c}\frac{\partial \boldsymbol{B}}{\partial t}, \tag{2}$$

$$\nabla \cdot \boldsymbol{B} = 0, \tag{3}$$

$$\nabla \times \boldsymbol{H} = \frac{1}{c}\frac{\partial \boldsymbol{D}}{\partial t}. \tag{4}$$

We consider nonmagnetic media, so that the magnetic and diamagnetic fields are equal, $\boldsymbol{B} = \boldsymbol{H}$. All of the material information is thus contained in the polarizaton $\mathbf{P}$ via the relation of $\boldsymbol{D} = \boldsymbol{E} + 4\pi\boldsymbol{P}$. Therefore the system of Maxwell equations reduces to

$$\Delta\boldsymbol{E} - \frac{\partial^2}{c^2\partial t^2}\boldsymbol{E} = -4\pi\nabla(\nabla\cdot\boldsymbol{P}) + 4\pi\frac{\partial^2}{c^2\partial t^2}\boldsymbol{P}. \tag{5}$$

We adopted the following mesoscopic approximation: the field propagating in the substrate medium with refractive index $n_{r,t}$ is scattered by a thin periodic superlattice. We take the metasurface part as the source of the wave propagating in the medium and derive the effective model. When the metasurface is placed at the interface between two substrates with refractive index $n_{r,t} = \sqrt{1+4\pi\chi_{r,t}}$, the corresponding z-dependent polarization term reads $\boldsymbol{P}(z,\boldsymbol{\rho},t) = \mathcal{H}(|z| \leqslant l_z/2)\boldsymbol{P}^{(3)}(\boldsymbol{E}) + [\mathcal{H}(z < \frac{-l_z}{2})\chi_r + \mathcal{H}(z > \frac{l_z}{2})\chi_t]\boldsymbol{E}(z,\boldsymbol{\rho},t)$. Here and below, the Heaviside function is $\mathcal{H}(\text{condition}) = \{1, \text{ when condition is true}; 0, \text{ when condition is false}\}$. In the zeroth approximation, the third-order nonlinear polarization is caused by the incident fields only, so that the corresponding nonlinear polarization is $\boldsymbol{P}^{(3)}_\gamma(\boldsymbol{E}) = \sum_{\alpha\beta\mu} X_{\gamma\alpha\beta\mu}(\boldsymbol{\rho})\mathcal{E}^{(1)}_\alpha\mathcal{E}^{(2)}_\beta\mathcal{E}^{(3)}_\mu e^{i(\mathrm{k}_s z + \boldsymbol{\kappa}_s\cdot\boldsymbol{\rho} - \omega_s t)}\boldsymbol{e}_\gamma$, where k_s, $\boldsymbol{\kappa}_s$ and ω_s are the wave vector and frequency of the nonlinear signal and $\mathcal{E}^{(i)}_\alpha$ is the αth Cartesian component of the ith incident wave $\boldsymbol{E}^{(i)}(\boldsymbol{r},t) = \boldsymbol{\mathcal{E}}^{(i)}e^{i\mathrm{k}_i z + \iota\boldsymbol{\kappa}_i\cdot\boldsymbol{\rho} - i\omega_i t}$. Without considering the rotation of each nanopillar, the susceptibility function $X_{\gamma\alpha\beta\mu}(\boldsymbol{\rho})$ can be represented as a sum of the susceptibilities of the individual primitives shifted in the xy plane $X_{\gamma\alpha\beta\mu}(\boldsymbol{\rho}) = \chi^{(3)}_{\gamma\alpha\beta\mu}\sum_{mn}\sum_{j=-N}^{N}\Omega(\boldsymbol{\rho} - \boldsymbol{\varrho}_{m+j,n})$, with location of nanopillars $\boldsymbol{\varrho}_{m+j,n} = \boldsymbol{\varrho}_{m,n} + j\boldsymbol{a}_1$, third-order susceptibility $\chi^{(3)}_{\gamma\alpha\beta\mu}$, and $N = (M-1)/2$. The indicator function $\Omega(\boldsymbol{\rho})$ describes the geometric shape of the rectangular nanopillar $\Omega(\boldsymbol{\rho}) = \mathcal{H}(|x| \leqslant l_x/2)\mathcal{H}(|y| \leqslant l_y/2)$. In order to discuss the third-order nonlinear process, each metallic or dielectric nanopillar of the metasurface is phenomenologically modeled as a six-level system in Fig. 1(c) originating from the three-level structure for each polarization coupled together [39–41]. The corresponding nonlinear susceptibility tensors for different nonlinear processes can be seen in Appendix B.

In the limit of ultrathin metasurface, we neglect the E_z and P_z components. The propagation of the electric field then satisfies

$$\Delta\boldsymbol{E}_{||} - \frac{n^2_{r,t}}{c^2}\ddot{\boldsymbol{E}}_{||} = 4\pi\mathcal{H}\left(|z| \leqslant \frac{l_z}{2}\right)\left[-\nabla(\nabla\cdot\boldsymbol{P}^{(3)}_{||}) + \frac{1}{c^2}\ddot{\boldsymbol{P}}^{(3)}_{||}\right]. \tag{6}$$

Fourier analysis is a powerful tool to derive an analytic description of the nonlinear metasurface system [26,42], while several theoretical works based on the Green's function method study second- and third-harmonic generation in the PB metasurface system [23,43,44]. In the $(\boldsymbol{\kappa},\omega)$ domain, the third-order nonlinear polarization is expressed in terms of the field $P^{(3)}_\gamma(z,\boldsymbol{\kappa},\omega') = \sum_{\alpha\beta\mu}\int d^2\boldsymbol{\kappa}'\tilde{X}_{\gamma\alpha\beta\mu}(\boldsymbol{\kappa}-\boldsymbol{\kappa}')E_{\alpha\beta\mu}(z,\boldsymbol{\kappa}',\omega')/(2\pi)^2$, with periodic susceptibility function $\tilde{X}_{\gamma\alpha\beta\mu}(\boldsymbol{\kappa}) = \sum_{j=-N}^{N}\sum_{m,n}\frac{\chi_{\gamma\alpha\beta\mu}(2\pi)^2}{Ma_1a_2/\tilde{\Omega}_j(\boldsymbol{\kappa})}\delta(\boldsymbol{\kappa}-\boldsymbol{G}_{mn})e^{-ij\boldsymbol{\kappa}\cdot\boldsymbol{a}_1}$, where

$\tilde{\Omega}_j(\boldsymbol{\kappa})$ is the Fourier transform of geometric shape factor $\Omega(\boldsymbol{\rho})$. Thus the polarization vector can be expanded as a sum over $\mathbf{Q}$—the first Brillouin zone ($\boldsymbol{\kappa}' \leqslant \boldsymbol{G}_{11}$)

$$P_\gamma^{(3)}(z,\boldsymbol{\rho},t) = N_0 \sum_{mn,\alpha\beta\mu} \int_{\mathbf{Q}} d^2\boldsymbol{\kappa}' d\omega' f_{mnj} E_{\alpha\beta\mu}(z,\boldsymbol{\kappa}',\omega') e^{i(\psi_{mnj}-\omega' t)}. \tag{7}$$

Here, $E_{\alpha\beta\mu}(z,\boldsymbol{\kappa}',\omega') = \mathcal{E}_\alpha^{(1)}\mathcal{E}_\beta^{(2)}\mathcal{E}_\mu^{(3)} e^{i\mathrm{k}_s z}\delta(\boldsymbol{\kappa}_s-\boldsymbol{\kappa}')\delta(\omega_s-\omega')$, and $\psi_{mnj} = \boldsymbol{G}_{mn}\cdot(\boldsymbol{\rho}-j\boldsymbol{a}_1)+\boldsymbol{\kappa}'\cdot\boldsymbol{\rho}$ describes the propagation phase, while $f_{mnj} = \frac{\tilde{\Omega}_j(\boldsymbol{G}_{mn})}{2\pi^2 M a_1 a_2}$ is the form factor for the jth nanopillar in the mn-th lattice primitive cell with the Fourier transform for the rectangular geometric shape factor $\tilde{\Omega}_j(\boldsymbol{G}_{mn})$. $N_0 = \frac{\chi_{\gamma\alpha\beta\mu}}{4\pi}$ is a normalization factor. The translational symmetry of the metasurface dictates the form of the solution given by

$$\boldsymbol{E}(z,\boldsymbol{\rho},t) = \sum_{m,n} \int_{\mathbf{Q}} d^2\boldsymbol{\kappa}' d\omega' d\mathrm{k} \tilde{\boldsymbol{E}}_{mn}(\mathrm{k},\boldsymbol{\kappa}',\omega') e^{i[\mathrm{k}z+(\boldsymbol{\kappa}'+\boldsymbol{G}_{mn})\cdot\boldsymbol{\rho}-\omega' t]}. \tag{8}$$

Let us focus on the $e^{i(\boldsymbol{G}_{mn}+\boldsymbol{\kappa}')\cdot\boldsymbol{\rho}}$ components. Since all the $\boldsymbol{G}_{mn}+\boldsymbol{\kappa}$ spatial components of $\tilde{E},\tilde{P}$ have the same subscripts m and n, these will be henceforth omitted. The corresponding thin polarization component $\mathcal{H}(|z|\leqslant l_z/2)\boldsymbol{P}^{(3)}(\boldsymbol{E})$ becomes $\sum_{\alpha\beta\mu}\frac{l_z}{4\pi} f_{mn} E_{\alpha\beta\mu}(z,\boldsymbol{\kappa}',\omega')$, where $f_{mn} = \sum_{j=-N}^{N} \chi_{\gamma\alpha\beta\mu} f_{mnj} e^{-ij\boldsymbol{G}_{mn}\cdot\boldsymbol{a}_1}/2\pi$. Dynamics equation (6) in the $\mathbf{k}$, ω space is

$$\tilde{C}'\tilde{E}_x = 4\pi\left(K_x^2-\frac{\omega^2}{c^2}\right)\tilde{P}_x + 4\pi K_x K_y \tilde{P}_y,$$
$$\tilde{C}'\tilde{E}_y = 4\pi\left(K_y^2-\frac{\omega^2}{c^2}\right)\tilde{P}_y + 4\pi K_y K_x \tilde{P}_x. \tag{9}$$

Here, wave vectors are $K_x = G_{mn,x}+\kappa_x'$, $K_y = G_{mn,y}+\kappa_y'$, $K_{||}^2 = K_x^2+K_y^2$, and $\tilde{C}' = -k_z^2 + \frac{\omega'^2 n_{r,t}^2}{c^2} - K_{||}^2$. We then derive the transmitted waves given by

$$E_\gamma = \sum_{\alpha\beta\mu,mn} F\left[\left(K_\gamma^2-\frac{\omega^2}{c^2}\right)\chi_{\gamma\alpha\beta\mu} + K_x K_y \chi_{\gamma\alpha\beta\mu}\right]\mathcal{E}_\alpha\mathcal{E}_\beta\mathcal{E}_\mu|_\Lambda. \tag{10}$$

Here, $\Lambda = \{\boldsymbol{\kappa}'\to\boldsymbol{\kappa}_s;\omega'\to\omega_s\}$, coordinate subscripts are $\{\gamma = x,y,\gamma' = y,x\}$, and the phase term is

$$F = \sum_{j=-N}^{N} F_z \frac{i l_z f_{mnj}}{C'} e^{-ij\boldsymbol{G}_{mn}\cdot\boldsymbol{a}_1 + i\boldsymbol{\kappa}'\cdot\boldsymbol{\rho} - i\omega' t},$$

while the propagation phase term along the z direction is $F_z = e^{i\sqrt{\frac{\omega'^2 n_{r,t}^2}{c^2}-K_{||}^2}z}\mathcal{H}(z>0) + e^{-i\sqrt{\frac{\omega'^2 n_{r,t}^2}{c^2}-K_{||}^2}z}\mathcal{H}(z<0)$ and $C' = \sqrt{\frac{\omega'^2 n_{r,t}^2}{c^2}-K_{||}^2}$. This transmitted wave can be formally written as $\boldsymbol{E} = \hat{T}(f_{mnj})\vdots\boldsymbol{\mathcal{E}}^{(1)}\boldsymbol{\mathcal{E}}^{(2)}\boldsymbol{\mathcal{E}}^{(3)}$ with the dyadic product symbol $\vdots$.

The matrix $\hat{R}(\phi_j)$ describing rotation by the constant incremental angle $\phi_j = \frac{\pi j}{2N+1}$ is given by $\hat{R}(\phi_j) = \begin{pmatrix}\cos(\phi_j) & -\sin(\phi_j)\\ \sin(\phi_j) & \cos(\phi_j)\end{pmatrix}$. The transmitted waves can be thus given by $\hat{R}(\phi_j)\boldsymbol{E} = \hat{T}[f_{mnj}(\phi_0)]\vdots[\hat{R}(\phi_j)\boldsymbol{\mathcal{E}}^{(1)}\hat{R}(\phi_j)\boldsymbol{\mathcal{E}}^{(2)}\hat{R}(\phi_j)\boldsymbol{\mathcal{E}}^{(3)}]$.

TABLE I. Chiral character of nonlinear metasurface. D.O., diffraction order.

Rotation	Input	Output (D.O.)	Phase gradient
Counterclockwise	σ_+	σ_+ (−1)	$\frac{-\lambda}{(2N+1)a_x}$
		σ_- (−2)	$\frac{-2\lambda}{(2N+1)a_x}$
Counterclockwise	σ_-	σ_- (+1)	$\frac{\lambda}{(2N+1)a_x}$
		σ_+ (+2)	$\frac{2\lambda}{(2N+1)a_x}$
Clockwise	σ_+	σ_+ (1)	$\frac{\lambda}{(2N+1)a_x}$
		σ_- (2)	$\frac{2\lambda}{(2N+1)a_x}$
Clockwise	σ_-	σ_- (−1)	$\frac{-\lambda}{(2N+1)a_x}$
		σ_+ (−2)	$\frac{-2\lambda}{(2N+1)a_x}$

Considering all the incident waves having the same polarization state we use the circularly polarized (CP) basis $\sigma_\pm = (\boldsymbol{e}_x \pm \iota\boldsymbol{e}_y)/\sqrt{2}$, and derive the explicit form for the scattering wave which yields

$$\begin{pmatrix} b_1\mathcal{E}_+^2\mathcal{E}_- + b_2\mathcal{E}_+^3 e^{-2i\phi_j} + b_3\mathcal{E}_+\mathcal{E}_-^2 e^{2i\phi_j} + b_4\mathcal{E}_-^3 e^{4i\phi_j} \\ b_1^*\mathcal{E}_-^2\mathcal{E}_+ + b_3^*\mathcal{E}_-\mathcal{E}_+^2 e^{-2i\phi_j} + b_2^*\mathcal{E}_-^3 e^{2i\phi_j} + b_4^*\mathcal{E}_+^3 e^{-4i\phi_j} \end{pmatrix}\Big|_\Lambda, \tag{11}$$

where the amplitude of the incident wave in the CP basis is written as $\boldsymbol{\mathcal{E}}_i = \{\mathcal{E}_+,\mathcal{E}_-\}$, the constant incremental rotation angle of the nanopillar is $\phi_j = \frac{\pi j}{2N+1}$, $\Lambda = \{\boldsymbol{\kappa}'\to\boldsymbol{\kappa}_s;\omega'\to\omega_s\}$, and the susceptibility-dependent coefficients $b_{1,2,3,4}$ are listed in Appendix A.

The scattering wave shown in Eq. (11) clearly reveals the PB-phase-induced manipulation of the wave front and polarization. Combining PB phase with the constant propagation as $\Xi_j = -\boldsymbol{G}_{mn}\cdot j\boldsymbol{a}_1 - \{0,2\phi_j,4\phi_j\}$, the PB phase of the individual nanopillars distributed uniformly between 0 and 2π leads to the destructive interferences $\sum_j e^{\pm i\Xi_j} \simeq 0$ as $\Xi_j \neq 0$. From this point of view, only scattered waves of order $m = 0,\pm1,\pm2$ have the possibility to be detected in the far field. Furthermore, the remaining part of the propagation phase, $(\mathbf{G}_{mn}+\boldsymbol{\kappa})\cdot\boldsymbol{\rho}$, yields the ordinary and generalized nonlinear Snell's law corresponding to different phase gradients as shown in Refs. [12–14,45]. In the meantime, the polarization of the scattered beams also relies on the polarization of the incident beams and symmetry of the metasurface structure as illustrated in Table I, which is consistent with previous theoretical and experimental works [12–14].

For a normal incident LP wave $\boldsymbol{\mathcal{E}}_i = \mathcal{E}\{1,1\}/\sqrt{2}$, the transmitted wave reveals the transmission of the linearly polarized wave in the zeroth diffraction order, while the transmitted waves of order ±2 are in the pure left CP (LCP) and right CP (RCP) states. On the other hand the transmitted wave in the ±1 diffraction order consists of a pair of oppositely handed elliptically polarized (EP) waves which depend on the magnitude of the wave vector and elements of the susceptibility tensor implicit in b_2, b_3 with azimuth angle $\frac{\mathrm{Arg}(b_2)+\mathrm{Arg}(b_3)}{2}$

and ellipticity angle $\pm\frac{1}{2}\arcsin\frac{|b_2|^2-|b_3|^2}{|b_2|^2+|b_3|^2}$, where Arg means the argument of a complex number. Therefore, by directly choosing a LP incident light, it becomes possible to have LCP, left (right) EP, LP, right (left) EP, and RCP light transmitted from diffraction order of -2 to diffraction order of 2. For experiment, the polarization state with diffraction order of ±1 can be controlled by changing the material or geometrical size of the nanopillars.

III. NONLINEAR SPECTRUM RECONSTRUCTION

The four-wave-mixing-based transmission of light assuming the same polarizations of incident beams can give four different different linear combinations of response function tensor elements, and it is not sufficient to distinguish each individual tensor component. The spectroscopic applications require a higher degree of control of the individual tensor components.

The heterodyne signal of the medium can be written as $t_{m,\pm}=\mathrm{Im}[\boldsymbol{E}^*_{m,\pm}(\omega_s)\boldsymbol{P}_{m,\pm}(\omega_s,\phi_j)]$, where m is the index of the scattering order, $\pm$ denotes the RCP or LCP component, and $\boldsymbol{E}^*_{m,\pm}(\omega_s)$ is the local oscillator field [35]. Therefore the spectra are decomposed into

$$\begin{aligned}
t_{0,r}&=\sum_{ijk}\mathrm{Im}[\mathcal{E}^*_{ijk}A_{xijk}-i\mathcal{E}_{ijk}B_{yijk}],\\
t_{1,r}&=\sum_{ijk}\mathrm{Im}[\mathcal{E}_{ijk}A_{xijk}-i\mathcal{E}^*_{ijk}B_{yijk}],\\
t_{1,l}&=\mathrm{Im}[\mathcal{E}_{123}(R_{xxxx}-R_{yyyy})],\\
t_{2,r}&=\mathrm{Im}[\mathcal{E}_{123}(R_{xxxx}+R_{yyyy})],
\end{aligned}\tag{12}$$

with the amplitude factors $\mathcal{E}_{123}=\prod_{i=1}^{3}(\mathcal{E}_{ix}-i\mathcal{E}_{iy})/\sqrt{2}$, $\mathcal{E}_{ijk}=\mathcal{E}_{1i}\mathcal{E}_{2j}\mathcal{E}_{3k}-i\mathcal{E}_{1i'}\mathcal{E}_{2j'}\mathcal{E}_{3k'}$, where $i,j,k=\{x,y\}$, $i',j',k'=\{y,x\}$, and the amplitude of the local oscillator field is set to be unity. The response functions A_{xijk}, B_{yijk}, R_{xxxx}, and R_{yyyy} are shown in Appendix A. In particular, the response functions of conjugate scattering components can be obtained by a complex conjugate of amplitude factors $\mathcal{E}_{123}$ and $\mathcal{E}_{ijk}$. Consequently, one can design a single measurement that reveals individual tensor components of the nonlinear response by adjusting the polarization state of each of the incident waves. In the following, the four-wave-mixing response is discussed as a theoretical representation of this experimental scheme.

To that end, we consider phase-matching case I, $\omega_s=\omega_1-\omega_2+\omega_3$, in Appendix B. By an exhaustive method, several different configurations of the polarization state of the incident waves can be used to realize the reconstruction of all the nonlinear susceptibility tensor components. As an example, we choose the polarization configuration of the incident waves shown on the right-hand side of Fig. 2(a): $\boldsymbol{\mathcal{E}}_1=\{1,1\}/\sqrt{2}$ (LP initially along the x axis), $\boldsymbol{\mathcal{E}}_2=\{0,\sqrt{2}\}$ (RCP), $\boldsymbol{\mathcal{E}}_3=\{i,i\}/\sqrt{2}$ (LP initially along the y axis), where the amplitude of the wave is set to be unity. By resolving these spectral functions [Eq. (12)], all the susceptibility components can be

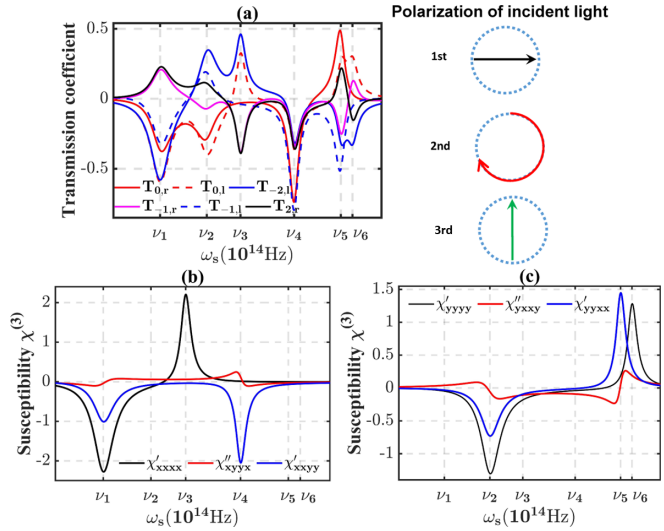

FIG. 2. The nonlinear spectrum vs the signal (new mode) frequency. The resonance frequencies depicted as vertical dashed lines are $\nu_1=\omega_x$, $\nu_2=\omega_y$, $\nu_3=\omega_{x'}-\omega_x$, $\nu_4=\omega_f-\omega_y$, $\nu_5=\omega_f-\omega_x$, and $\nu_6=\omega_{y'}-\omega_y$ illustrated by the level scheme in Fig. 1(c). The frequency of the incident wave is $\omega_1=\omega_2=600$ THz. (a) One-dimensional spectrum of heterodyne signals from six transmission channels. The figure in the right side of (a) denotes the polarization configuration of three incident light in the four-wave-mixing process. (b) and (c) The real and imaginary parts of the nonlinear effective susceptibility tensor components reconstructed from the spectrum in (a).

reconstructed as

$$\begin{aligned}
\chi'_{xxxx}&=\sqrt{2}(t_{0,l}+t_{1,r}-t_{-1,r}-t_{-2,l}),\\
\chi'_{yyyy}&=\sqrt{2}(t_{0,l}-t_{1,r}+t_{-1,r}-t_{-2,l}),\\
\chi'_{xxyy}&=(t_{0,l}+t_{0,r}+t_{-1,l}+t_{1,r}+t_{-1,r}+t_{-2,l})/\sqrt{2},\\
\chi''_{xyyx}&=(t_{0,l}-t_{0,r}-t_{-1,l}+t_{1,r}+t_{-1,r}+t_{-2,l})/\sqrt{2},\\
\chi''_{yxxy}&=(t_{0,l}-t_{0,r}+t_{-1,l}-t_{1,r}-t_{-1,r}+t_{-2,l})/\sqrt{2},\\
\chi'_{yyxx}&=(t_{0,l}+t_{0,r}-t_{-1,l}-t_{1,r}-t_{-1,r}+t_{-2,l})/\sqrt{2}.
\end{aligned}$$

Here, susceptibility elements are written as $\chi_{\gamma\alpha\beta\mu}=\chi'_{\gamma\alpha\beta\mu}+i\chi''_{\gamma\alpha\beta\mu}$. In Fig. 2(a), the dispersion curves of six nonzero transmitted signals denote different linear combinations of the tensor elements. The corresponding six resonant peaks around ν_j $(j=1,\ldots,6)$ correspond to the six transitions depicted in the level scheme in Fig. 1(c). After combining these six signals, the reconstructed 1D spectra of each of the components are illustrated in Figs. 2(b) and 2(c). Figure 2(b) shows resonances at frequencies ν_1, ν_3, ν_4 by depicting the real part of χ_{xxxx} and χ_{xxyy} and the imaginary part of χ_{xyyx} vs the signal frequency ω_s. Similarly, we observe ν_2, ν_5, ν_6 resonances by depicting the real part of χ_{yyyy} and χ_{yyxx} and the imaginary part of χ_{yxxy} in Fig. 2(c). Therefore Fig. 2 provides the matter information in the form of the six resonances permitted by our model in Fig. 1(c) along with their lineshapes corresponding to dephasing timescales due to electron-phonon scattering. This information obtained by studies of the $\chi^{(3)}$ tensor is certainly superior to the linear response, which is capable of

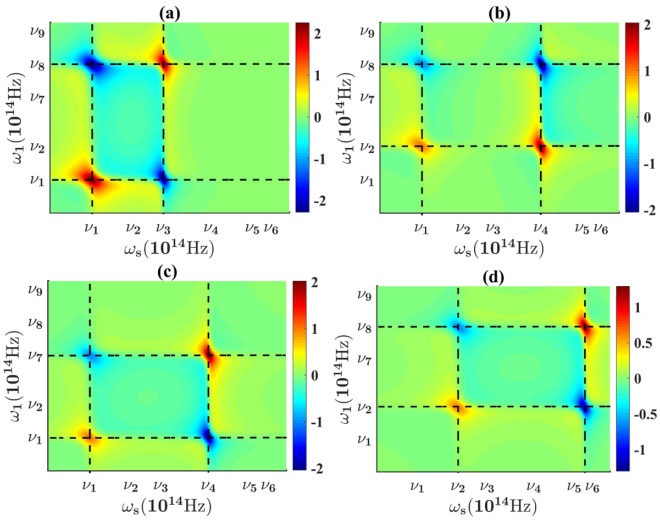

FIG. 3. Two-dimensional spectrum of the susceptibility components χ_{xxxx} (a), χ_{xyyx} (b), χ_{xxyy} (c), and χ_{yyyy} (d) displayed vs the frequency of the signal field and one of the incoming fields. The diagonal ($\omega_s = \omega_1 = \nu_j$) and off-diagonal ($\omega_s = \nu_i$, $\omega_1 = \nu_j$, $i \neq j$, $i, j = 1, \ldots, 6$) cross peaks indicate the stationary and transient oscillating charge corresponding to plasmonic occupation (population) and coherences, respectively, between the resonant transitions indicated in Fig. 1(c). Simulation parameters are as follows: $\omega_2 = 600$ THz, $\nu_7 = \omega_2 + (\omega_x - \omega_y)$, $\nu_8 = \omega_2$, and $\nu_9 = \omega_2 + (\omega_y - \omega_x)$. The configurations of the polarization state of the incident waves are the same as those in Fig. 2.

explaining $|x\rangle - |g\rangle$ and $|y\rangle - |g\rangle$ lower-energy single photon resonances only. On the other hand, the same set of measurements that is responsible for the signal in Fig. 2 is capable of revealing more complex material information related to the stationary and transient plasmonic charge density. To obtain such information, one can display the susceptibility tensor as a function of signal frequency ω_s and one of the incoming field frequencies, e.g., ω_1. The corresponding reconstructed multidimensional spectra of the six nonlinear susceptibility tensor components are shown in Fig. 3. The interpretation of the 2D spectra is similar to that of the photon echo [35]. The diagonal peaks where $\omega_s = \omega_1 = \nu_j$ ($j = 1, \ldots, 9$) reveal the stationary charge density corresponding to localized plasmon mode occupation number. The cross peaks at $\omega_s = \nu_j$, $\omega_1 = \nu_i$, $i = 1, \ldots, 6$, $i \neq j$ correspond to the transient oscillating delocalized plasmonic charge density emerging due to the coupling of two spatial excitation modes. For example, in Fig. 3(a), the diagonal peak at $\{\omega_s = \omega_1 = \nu_1\}$ represents the transition between the excited state $|x\rangle$ and the ground state $|g\rangle$. The cross peaks at $\{\omega_s = \nu_3, \omega_1 = \nu_1\}$ illustrate the coupling between transition 1—excited state $|x\rangle$ and ground state $|g\rangle$—and transition 2—excited state $|x\rangle$ and doubly excited state $|x'\rangle$. One can obtain material information for different localized and transient plasmonic charge densities by varying other incoming field frequencies, e.g., ω_2 and ω_3.

IV. CONCLUSIONS

In summary, we investigated a four-wave-mixing signal generated from a PB metasurface by multichannel polarization manipulation. A model for a nonlinear PB metasurface is gives an analytical description of the polarization-sensitive transmission. We find that the LP incident beams can be converted into different polarizations by five channels in a single measurement using a PB metasurface with relatively simple 1D unit cells. Unlike second- or third-harmonic emission, four-wave mixing provides the signal in the same frequency range as the incident beams. This mechanism provides a way to realize the multichannel optical information transmission for imaging [11,20,22,46] and information encoding and quantum cryptography [30,47–50]. Moreover, we showed that careful selection of the fundamental wave with different polarizations allows one to obtain phase information in all components of the third-order nonlinear susceptibility tensor by polarization selection of the real and imaginary parts. Furthermore, we demonstrated that this phase-sensitive polarization manipulation provides a deep level of spectroscopic information of the nanostructure. The 1D spectra allow one to extract the resonant energy structure and dephasing times. The 2D signals can be used to track stationary and transient charge density distributions that correspond to localized as well as delocalized plasmonic modes. These theoretical predictions establish the metasurface as a high-precision tool for multidimensional spectroscopy characterization of anisotropic and topological nanomaterials.

ACKNOWLEDGMENTS

Z.G. thanks S. Jiang and G. Zhu for valuable discussions. Z.G. and K.E.D. gratefully acknowledge the support from the National Natural Science Foundation of China (Grant No. 11934011), the Zijiang Endowed Young Scholar Fund, East China Normal University, and the Overseas Expertise Introduction Project for Discipline Innovation (111 Project, B12024). K.E.D. is grateful for the support of Fédération Doeblin. P.G. acknowledges funding from the European Research Council (ERC) under the European Union's Horizon 2020 research and innovation program (Grant Agreement No. 639109). G.L. acknowledges the financial support from the National Natural Science Foundation of China (Grants No. 91950114 and No. 11774145), the Guangdong Provincial Innovation and Entrepreneurship Project (Grant No. 2017ZT07C071), and the Natural Science Foundation of Shenzhen Innovation Commission (Grant No. JCYJ20200109140808088).

APPENDIX A: TRANSMISSION COEFFICIENTS

In order to show a simple result without effecting the physical result, we set $\theta' = 0$, and the coefficients of the third-order signal are

$$b_1 = \frac{3F}{4}\left[a_1'\left(K_x^2 - \frac{\omega^2}{c^2}\right) + a_4' K_x K_y + a_2'\left(K_y^2 - \frac{\omega^2}{c^2}\right)\right],$$

$$b_2 = \frac{F}{4}\left[a_3'\left(K_x^2 - \frac{\omega^2}{c^2}\right) + a_7' K_x K_y + a_5'\left(K_y^2 - \frac{\omega^2}{c^2}\right)\right],$$

$$b_3 = \frac{3F}{4}\left[a_1'^{*}\left(K_x^2 - \frac{\omega^2}{c^2}\right) + a_6' K_x K_y - a_2'^{*}(K_y^2 - \frac{\omega^2}{c^2})\right],$$

$$b_4 = \frac{F}{4}\left[a_3'^{*}\left(K_x^2 - \frac{\omega^2}{c^2}\right) - a_4'^{*}K_xK_y - a_5'^{*}\left(K_y^2 - \frac{\omega^2}{c^2}\right)\right],$$

where

$$a_1' = \chi_{xxxx} + i\chi_{xxxy} + \chi_{xxyy} + i\chi'_{xyyy},$$
$$a_2' = -i\chi_{xxxy} + \chi_{xxyy} - i\chi_{xyyy} + \chi_{yyyy},$$
$$a_3' = \chi_{xxxx} + 3i\chi_{xxxy} - 3\chi_{xxyy} - i\chi_{xyyy},$$
$$a_4' = -i\chi_{xxxx} + 2\chi_{xxxy} + 2\chi_{xyyy} + i\chi_{yyyy},$$
$$a_5' = -i\chi_{xxxy} + 3\chi_{xxyy} + 3i\chi_{xyyy} - \chi_{yyyy},$$
$$a_6' = -i\chi_{xxxx} - 2i\chi'_{xxyy} - i\chi_{yyyy},$$
$$a_7' = -i\chi_{xxxx} + 4\chi_{xxxy} + 6i\chi_{xxyy} - 4\chi_{xyyy} - i\chi_{yyyy}.$$

The response functions are defined as

$$A_{xxxx} = (3\chi_{xxxx} + \chi_{xxyy} + \chi_{xyxy} + \chi_{xyyx})/(8\sqrt{2}),$$
$$A_{xyxy} = (3\chi_{xyxy} + \chi_{xxxx} - \chi_{xxyy} - \chi_{xyyx})/(8\sqrt{2}),$$
$$A_{xyyx} = (3\chi_{xyyx} + \chi_{xxxx} - \chi_{xxyy} - \chi_{xyxy})/(8\sqrt{2}),$$
$$A_{xxyy} = (3\chi_{xxyy} + \chi_{xxxx} - \chi_{xyxy} - \chi_{xyyx})/(8\sqrt{2}),$$
$$B_{yyyy} = (3\chi_{yyyy} + \chi_{yxxy} + \chi_{yxyx} + \chi_{yyxx})/(8\sqrt{2}),$$
$$B_{yxyx} = (3\chi_{yxyx} - \chi_{yxxy} - \chi_{yyxx} + \chi_{yyyy})/(8\sqrt{2}),$$
$$B_{yyxx} = (3\chi_{yyxx} - \chi_{yxxy} - \chi_{yxyx} + \chi_{yyyy})/(8\sqrt{2}),$$
$$R_{xxxx} = [(\chi_{xxxx} - (\chi_{xxyy} + \chi_{xyxy} + \chi_{xyyx})]/4,$$
$$R_{yyyy} = [(\chi_{yyyy} - (\chi_{yxxy} + \chi_{yxyx} + \chi_{yyxx})]/4.$$

APPENDIX B: THIRD-ORDER NONLINEAR SUSCEPTIBILITY FOR A SIX-LEVEL SYSTEM

An energy level diagram of the birefringent nanopillars is shown in Fig. 1(c). The elements of the susceptibility tensor of four-wave mixing satisfy $\chi_{xxxy} = \chi_{xxyx} = \chi_{xyxx} = \chi_{xyyy} = \chi_{yxxx} = \chi_{yxyy} = \chi_{yyxy} = \chi_{yyyx} = 0$. The notation is as follows: Γ_x, Γ_y, Γ_{xx}, Γ_{yy}, Γ_{xy}, Γ_{yx}, $\Gamma_{x,y}$, $\Gamma_{y,x}$, $\Gamma_{x',x}$, $\Gamma_{y',x}$, $\Gamma_{f,x}$, $\Gamma_{x',y}$, $\Gamma_{y',y}$, and $\Gamma_{f,y}$ are the decay parameters of $|x\rangle\langle g|$, $|y\rangle\langle g|$, $|x'\rangle\langle g|$, $|y'\rangle\langle g|$, $|f\rangle\langle g|$, $|x\rangle\langle y|$, $|y\rangle\langle x|$, $|x'\rangle\langle x|$, $|y'\rangle\langle x|$, $|f\rangle\langle x|$, $|x'\rangle\langle y|$, $|y'\rangle\langle y|$, and $|f\rangle\langle y|$. In the simulation, we set all the decay parameters to be 10 THz; $\omega_x = 460$ THz, $\omega_y = 500$ THz, and $\mu_y = 0.6\mu_x$.

For the phase matching $\omega_s = \omega_1 - \omega_2 + \omega_3$, which we refer to as case I, we have the following three different probabilities for the six-level system shown in Fig. 1(c).

Probability 1:

$$\chi_{xxxx} = \frac{N_0\mu_x^4}{(\omega_s - \omega_x + i\Gamma_x)(\omega_1 - \omega_2 + i\Gamma_{gg})(\omega_1 - \omega_x + i\Gamma_x)},$$
$$\chi_{xxyy} = \frac{N_0\mu_x^2\mu_y^2}{(\omega_s - \omega_x + i\Gamma_x)(\omega_1 - \omega_2 + i\Gamma_{gg})(\omega_1 - \omega_y + i\Gamma_y)},$$
$$\chi_{yyyy} = \frac{N_0\mu_y^4}{(\omega_s - \omega_y + i\Gamma_y)(\omega_1 - \omega_2 + i\Gamma_{gg})(\omega_1 - \omega_y + i\Gamma_y)},$$
$$\chi_{yyxx} = \frac{N_0\mu_x^2\mu_y^2}{(\omega_s - \omega_y + i\Gamma_y)(\omega_1 - \omega_2 + i\Gamma_{gg})(\omega_1 - \omega_x + i\Gamma_x)}.$$

Probability 2:

$$\chi_{xxxx} = \frac{-N_0\mu_x^4}{(\omega_s - \omega_{x'x} + i\Gamma_{x',x})(\omega_1 - \omega_2 + i\Gamma_{x,x})(\omega_1 - \omega_x + i\Gamma_x)},$$
$$\chi_{yyxx} = \frac{-N_0\mu_x^2\mu_y^2}{(\omega_s - \omega_{fx} + i\Gamma_{f,x})(\omega_1 - \omega_2 + i\Gamma_{x,x})(\omega_1 - \omega_x + i\Gamma_x)},$$
$$\chi_{yyyy} = \frac{-N_0\mu_y^4}{(\omega_s - \omega_{y'y} + i\Gamma_{y',y})(\omega_1 - \omega_2 + i\Gamma_{y,y})(\omega_1 - \omega_y + i\Gamma_y)},$$
$$\chi_{xxyy} = \frac{-N_0\mu_x^2\mu_y^2}{(\omega_s - \omega_{f'y} + i\Gamma_{f',y})(\omega_1 - \omega_2 + i\Gamma_{y,y})(\omega_1 - \omega_y + i\Gamma_y)},$$

$$\chi_{yxxy} = \frac{-N_0\mu_x^2\mu_y^2}{(\omega_s - \omega_{f'x} + i\Gamma_{f',x})(\omega_1 - \omega_2 - \omega_{yx} + i\Gamma_{y,x})(\omega_1 - \omega_y + i\Gamma_y)},$$
$$\chi_{xyyx} = \frac{-N_0\mu_x^2\mu_y^2}{(\omega_s - \omega_{fy} + i\Gamma_{f,y})(\omega_1 - \omega_2 - \omega_{xy} + i\Gamma_{x,y})(\omega_1 - \omega_x + i\Gamma_x)}.$$

Here, $\omega_{x'} - \omega_x = \omega_{x'x}$, $\omega_f - \omega_x = \omega_{fx}$, $\omega_{f'} - \omega_x = \omega_{f'x}$, $\omega_y - \omega_x = \omega_{yx}$, $\omega_{y'} - \omega_y = \omega_{y'y}$, $\omega_{f'} - \omega_y = \omega_{f'y}$, $\omega_f - \omega_y = \omega_{fy}$, and $\omega_x - \omega_y = \omega_{xy}$.

Probability 3:

$$\chi_{xxxx} = \frac{N_0\mu_x^4}{(\omega_s-\omega_x+i\Gamma_x)(\omega_1-\omega_2+i\Gamma_{x,x})(\omega_1-\omega_x+i\Gamma_x)},$$
$$\chi_{xyyx} = \frac{N_0\mu_x^2\mu_y^2}{(\omega_s-\omega_x+i\Gamma_x)(\omega_1-\omega_2-\omega_{xy}+i\Gamma_{x,y})(\omega_1-\omega_x+i\Gamma_x)},$$
$$\chi_{yyyy} = \frac{N_0\mu_y^4}{(\omega_s-\omega_y+i\Gamma_y)(\omega_1-\omega_2+i\Gamma_{y,y})(\omega_1-\omega_y+i\Gamma_y)},$$
$$\chi_{yxxy} = \frac{N_0\mu_x^2\mu_y^2}{(\omega_s-\omega_y+i\Gamma_y)(\omega_1-\omega_2+\omega_{xy}+i\Gamma_{y,x})(\omega_1-\omega_y+i\Gamma_y)}.$$

For the phase matching $\omega_s = -\omega_1+\omega_2+\omega_3$, which we refer to as case II, we have the following three different probabilities for the six-level system shown in Fig. 1(c).

Probability 1:

$$\chi_{xxxx} = \frac{-N_0\mu_x^4}{(\omega_s-\omega_{x'x}+i\Gamma_{x',x})(\omega_2-\omega_1+i\Gamma_{x,x})(\omega_x-\omega_1+i\Gamma_x^*)},$$
$$\chi_{yyxx} = \frac{-N_0\mu_x^2\mu_y^2}{(\omega_s-\omega_{fx}+i\Gamma_{f,x})(\omega_2-\omega_1+i\Gamma_{x,x})(\omega_x-\omega_1+i\Gamma_x^*)},$$
$$\chi_{yyyy} = \frac{-N_0\mu_y^4}{(\omega_s-\omega_{y'y}+i\Gamma_{y',y})(\omega_2-\omega_1+i\Gamma_{y,y})(\omega_y-\omega_1+i\Gamma_y^*)},$$
$$\chi_{xxyy} = \frac{-N_0\mu_x^2\mu_y^2}{(\omega_s-\omega_{f'y}+i\Gamma_{f',y})(\omega_2-\omega_1+i\Gamma_{y,y})(\omega_y-\omega_1+i\Gamma_y^*)},$$
$$\chi_{yxyx} = \frac{-N_0\mu_x^2\mu_y^2}{(\omega_s-\omega_{f'x}+i\Gamma_{f',x})(-\omega_1+\omega_2-\omega_{yx}+i\Gamma_{y,x})(-\omega_1+\omega_x+i\Gamma_x^*)},$$
$$\chi_{xyxy} = \frac{-N_0\mu_x^2\mu_y^2}{(\omega_s-\omega_{fy}+i\Gamma_{f,y})(-\omega_1+\omega_2-\omega_{xy}+i\Gamma_{x,y})(-\omega_1+\omega_y+i\Gamma_y^*)}.$$

Probability 2:

$$\chi_{xxxx} = \frac{N_0\mu_x^4}{(\omega_s-\omega_x+i\Gamma_x)(-\omega_1+\omega_2+i\Gamma_{gg})(-\omega_1+\omega_x+i\Gamma_x^*)},$$
$$\chi_{yyxx} = \frac{N_0\mu_x^2\mu_y^2}{(\omega_s-\omega_y+i\Gamma_y)(-\omega_1+\omega_2+i\Gamma_{gg})(-\omega_1+\omega_x+i\Gamma_x^*)},$$
$$\chi_{yyyy} = \frac{N_0\mu_y^4}{(\omega_s-\omega_y+i\Gamma_y)(-\omega_1+\omega_2+i\Gamma_{gg})(-\omega_1+\omega_y+i\Gamma_y^*)},$$
$$\chi_{xxyy} = \frac{N_0\mu_x^2\mu_y^2}{(\omega_s-\omega_x+i\Gamma_x)(-\omega_1+\omega_2+i\Gamma_{gg})(-\omega_1+\omega_y+i\Gamma_y^*)}.$$

Probability 3:

$$\chi_{xxxx} = \frac{N_0\mu_x^4}{(\omega_s-\omega_x+i\Gamma_x)(-\omega_1+\omega_2+i\Gamma_{x,x})(-\omega_1+\omega_x+i\Gamma_x^*)},$$
$$\chi_{yxyx} = \frac{N_0\mu_x^2\mu_y^2}{(\omega_s-\omega_y+i\Gamma_y)(-\omega_1+\omega_2-\omega_{yx}+i\Gamma_{y,x})(-\omega_1+\omega_x+i\Gamma_x^*)},$$
$$\chi_{yyyy} = \frac{N_0\mu_y^4}{(\omega_s-\omega_y+i\Gamma_y)(-\omega_1+\omega_2+i\Gamma_{y,y})(-\omega_1+\omega_y+i\Gamma_y^*)},$$
$$\chi_{xyxy} = \frac{N_0\mu_x^2\mu_y^2}{(\omega_s-\omega_x+i\Gamma_x)(-\omega_1+\omega_2-\omega_{xy}+i\Gamma_{x,y})(-\omega_1+\omega_y+i\Gamma_y^*)}.$$

For the phase matching $\omega_s = \omega_1+\omega_2-\omega_3$, which we refer to as case III, we have the following two different probabilities for the six-level system shown in Fig. 1(c).

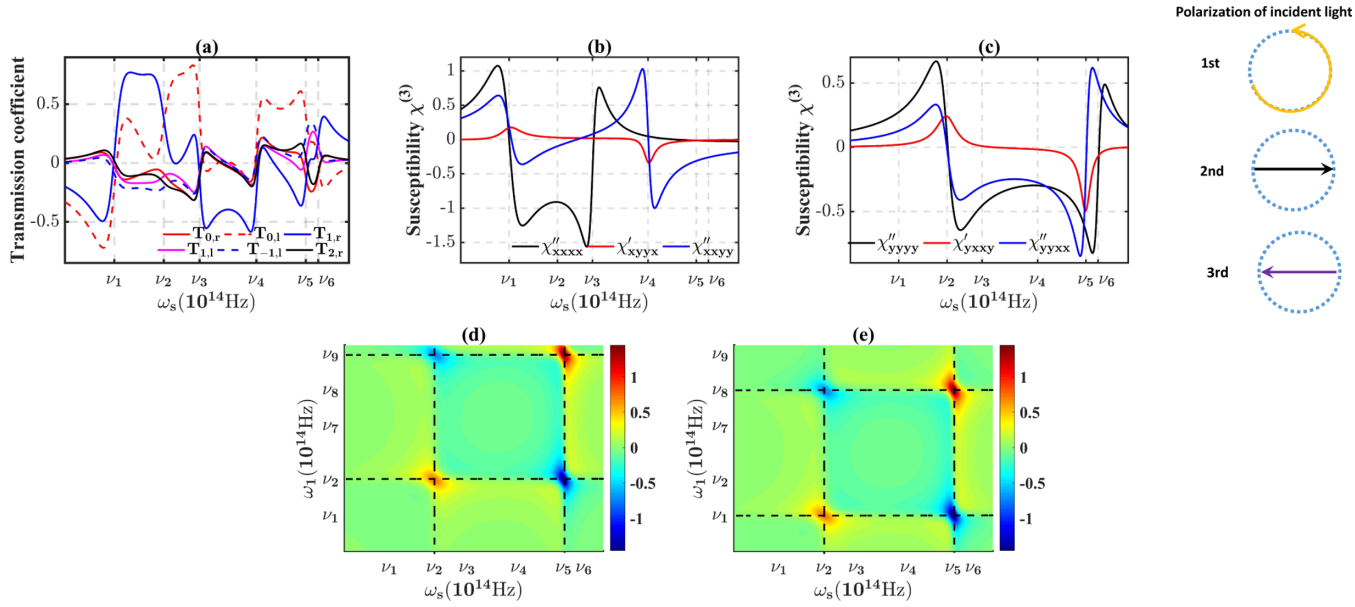

FIG. 4. The nonlinear spectrum vs the signal (new mode) frequency for phase-matching case I. The resonance frequencies shown here are the same as those in Figs. 2 and 3. (a) One-dimensional spectrum of heterodyne signals from six transmission channels. (b) and (c) The real and imaginary parts of the nonlinear effective susceptibility tensor components reconstructed from the spectrum in (a). (d) and (e) Two-dimensional spectrum of the susceptibility components χ_{yxxy} and χ_{yyxx} displayed vs the frequency of the signal field and one of the incoming fields. (a)–(c) supplement Fig. 2 in the main text, and (d) and (e) supplement Fig. 3 in the main text.

Probability 1:

$$\chi_{xxxx} = \frac{N_0\mu_x^4}{(\omega_s - \omega_x + i\Gamma_x)(\omega_1 + \omega_2 - \omega_{x'} + i\Gamma_{x'})(\omega_1 - \omega_x + i\Gamma_x)},$$

$$\chi_{yxyx} = \frac{N_0\mu_x^2\mu_y^2}{(\omega_s - \omega_y + i\Gamma_y)(\omega_1 + \omega_2 - \omega_f + i\Gamma_f)(\omega_1 - \omega_x + i\Gamma_x)},$$

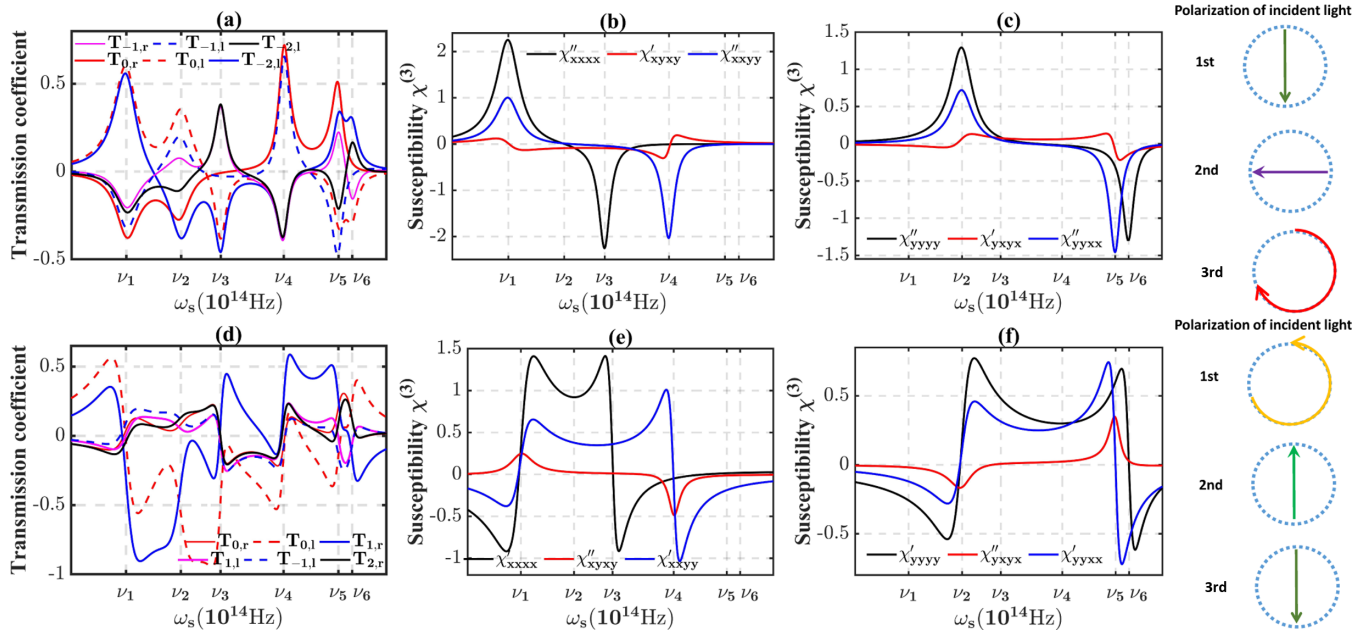

FIG. 5. The nonlinear spectrum vs frequency for phase-matching case II. The frequency of incident light is $\omega_1 = \omega_2 = 600$ THz. (a) and (d) One-dimensional spectrum of six nonvanishing components for two different combinations of the polarization state of incident light. The polarization state of incident light is shown to the right of each row. (b), (c), (e), and (f) The real and imaginary parts of the nonlinear susceptibility tensor components reconstructed from the spectra in (a) and (d).

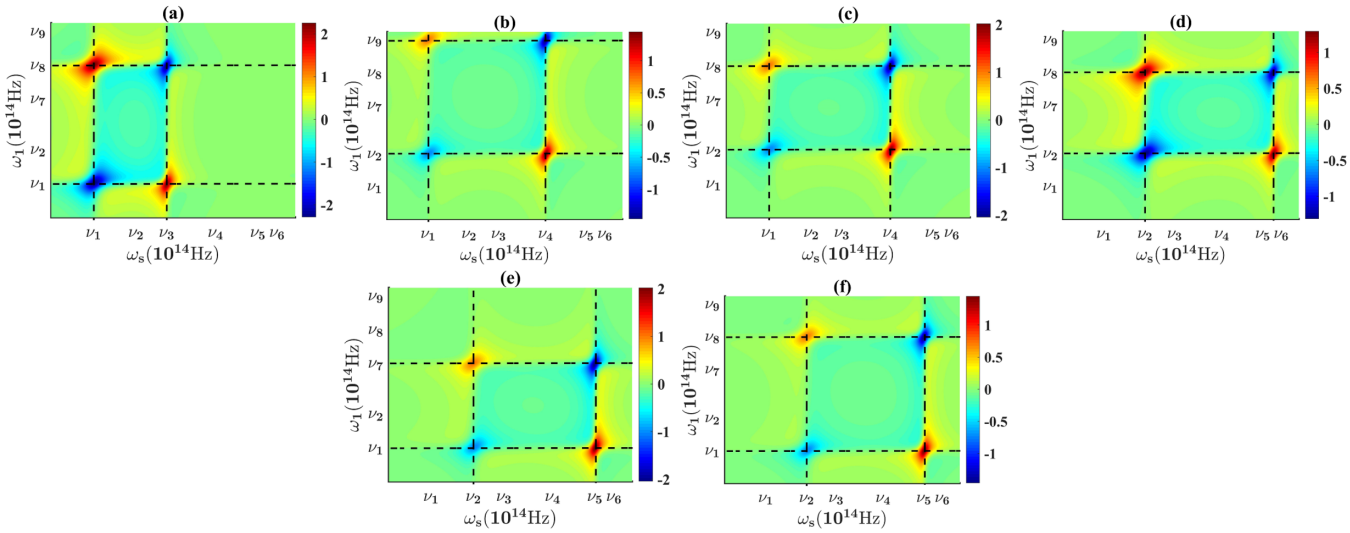

FIG. 6. Two-dimensional spectrum of components χ_{xxxx} (a), χ_{xyyx} (b), χ_{xxyy} (c), χ_{yyyy} (d), χ_{yxxy} (e), and χ_{yyxx} (f) with $\omega_2 = 600$ THz for phase-matching case II.

$$\chi_{xyyx} = \frac{N_0\mu_x^2\mu_y^2}{(\omega_s - \omega_x + i\Gamma_x)(\omega_1 + \omega_2 - \omega_f + i\Gamma_f)(\omega_1 - \omega_x + i\Gamma_x)},$$

$$\chi_{yyyy} = \frac{N_0\mu_y^4}{(\omega_s - \omega_y + i\Gamma_y)(\omega_1 + \omega_2 - \omega_{y'} + i\Gamma_{y'})(\omega_1 - \omega_y + i\Gamma_y)},$$

$$\chi_{xyxy} = \frac{N_0\mu_x^2\mu_y^2}{(\omega_s - \omega_x + i\Gamma_x)(\omega_1 + \omega_2 - \omega_{f'} + i\Gamma_{f'})(\omega_1 - \omega_y + i\Gamma_y)},$$

$$\chi_{yxxy} = \frac{N_0\mu_x^2\mu_y^2}{(\omega_s - \omega_y + i\Gamma_y)(\omega_1 + \omega_2 - \omega_{f'} + i\Gamma_{f'})(\omega_1 - \omega_y + i\Gamma_y)}.$$

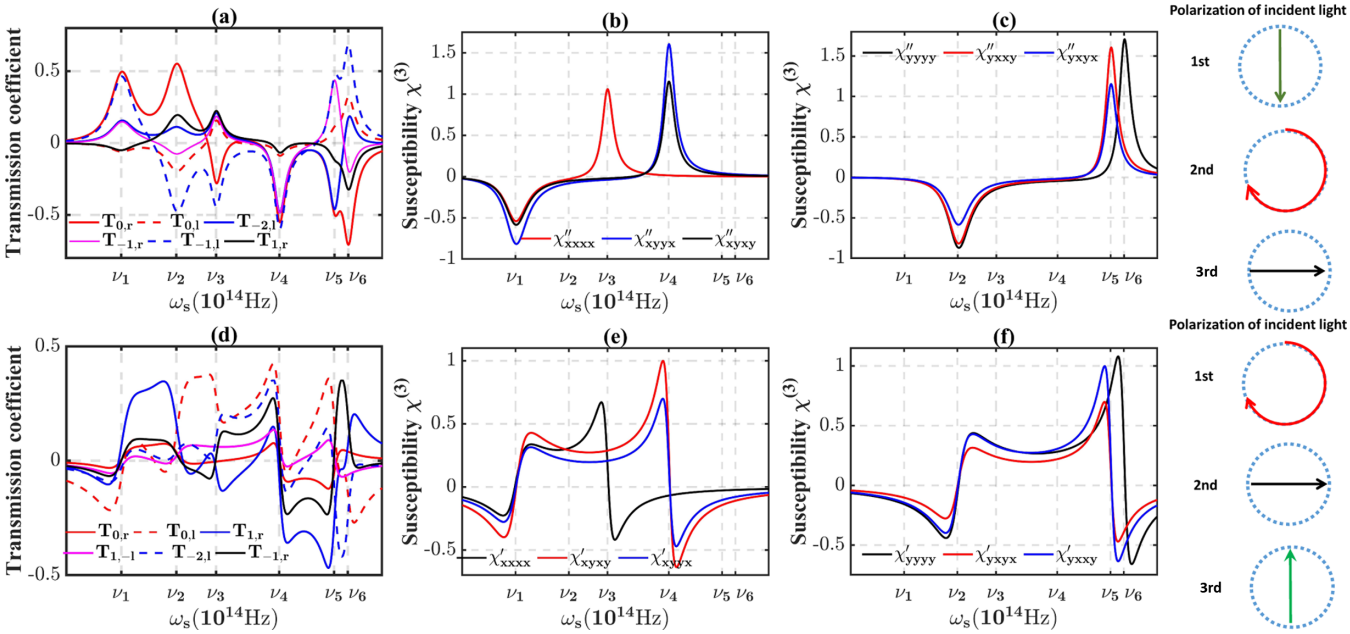

FIG. 7. The nonlinear spectrum vs frequency for phase-matching case III. The frequency of incident light is $\omega_1 = \omega_2 = 600$ THz. (a) and (d) One-dimensional spectrum of six nonvanishing components for two different combinations of the polarization state of incident light. The polarization state of incident light is shown to the right of each row. (b), (c), (e), and (f) The real and imaginary parts of the nonlinear susceptibility tensor components reconstructed from the spectra in (a) and (d).

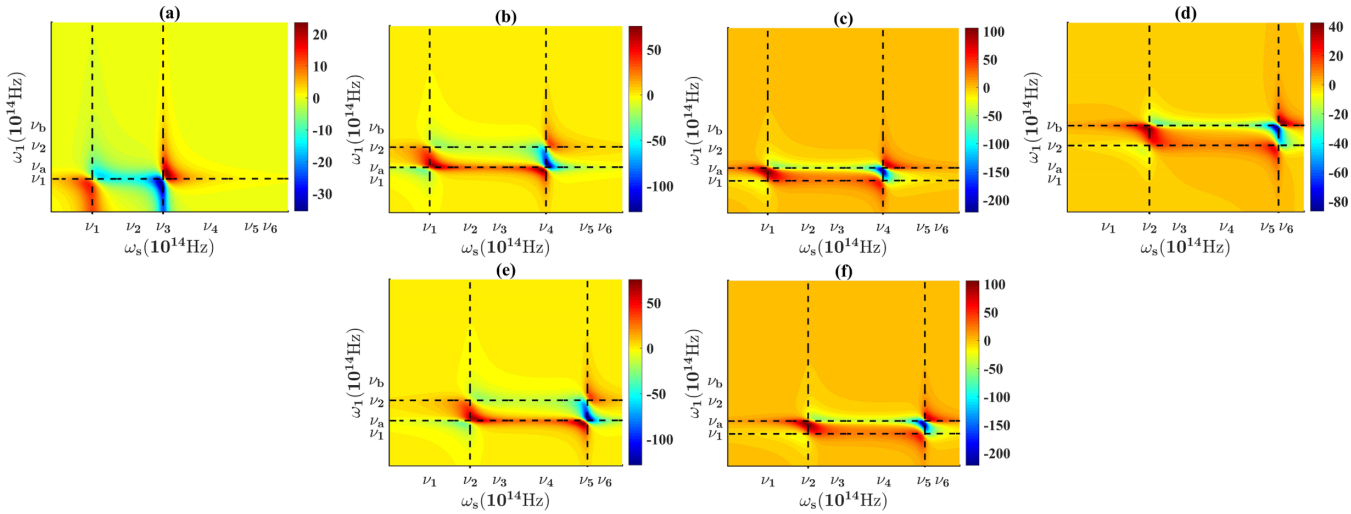

FIG. 8. Two-dimensional spectrum of components χ_{xxxx} (a), χ_{xyyx} (b), χ_{xxyy} (c), χ_{yyyy} (d), χ_{yxxy} (e), and χ_{yyxx} (f) with $\omega_2 = 600$ THz for phase-matching case III.

Probability 2:

$$\chi_{xxxx} = \frac{-N_0\mu_x^4}{(\omega_s - \omega_{x'x} + i\Gamma_{x',x})(\omega_1 + \omega_2 - \omega'_x + i\Gamma_{x'})(\omega_1 - \omega_x + i\Gamma_x)},$$

$$\chi_{yxyx} = \frac{-N_0\mu_x^2\mu_y^2}{(\omega_s - \omega_{fx} + i\Gamma_{f,x})(\omega_1 + \omega_2 - \omega_f + i\Gamma_f)(\omega_1 - \omega_x + i\Gamma_x)},$$

$$\chi_{yxxy} = \frac{-N_0\mu_x^2\mu_y^2}{(\omega_s - \omega_{f'x} + i\Gamma_{f',x})(\omega_1 + \omega_2 - \omega'_f + i\Gamma_{f'})(\omega_1 - \omega_y + i\Gamma_y)},$$

$$\chi_{yyyy} = \frac{-N_0\mu_y^4}{(\omega_s - \omega_{y'y} + i\Gamma_{y',y})(\omega_1 + \omega_2 - 2\omega'_y + i\Gamma_{y'})(\omega_1 - \omega_y + i\Gamma_y)},$$

$$\chi_{xyxy} = \frac{-N_0\mu_x^2\mu_y^2}{(\omega_s - \omega_{f'y} + i\Gamma_{f',y})(\omega_1 + \omega_2 - \omega_{f'} + i\Gamma_{f'})(\omega_1 - \omega_y + i\Gamma_y)},$$

$$\chi_{xyyx} = \frac{-N_0\mu_x^2\mu_y^2}{(\omega_s - \omega_{fy} + i\Gamma_{f,y})(\omega_1 + \omega_2 - \omega_f + i\Gamma_f)(\omega_1 - \omega_x + i\Gamma_x)}.$$

APPENDIX C: THE FOUR-WAVE-MIXING RESPONSE FOR PHASE-MATCHING CASES I—III

In this Appendix, we show the reconstructed four-wave-mixing response for different phase-matching cases. For phase matching I, Figs. 4(a)–4(c) show the heterodyne signals and the corresponding reconstructed 1D four-wave-mixing response. They give the other half of response to supplement Fig. 2 in the main text. Figures 4(d) and 4(e) give two components of response to supplement Fig. 3 in the main text. The one- and two-dimensional spectrum for the phase-matching II and III are shown in Figs. 5, 6 and 7, 8, respectively.

[1] C. A. V. Cruz, H. Shaban, A. Kress, N. Bertaux, S. Monneret, M. Mavrakis, J. Savatier, and S. Brasselet, Quantitative nanoscale imaging of orientational order in biological filaments by polarized superresolution microscopy, Proc. Natl. Acad. Sci. USA **113**, E820 (2016).

[2] F. Sanda and S. Mukamel, Novel coherent two-dimensional optical spectroscopy probes of chirality exchange and fluctuations in molecules, J. Chem. Phys. **135**, 194201 (2011).

[3] S. Kujala, B. K. Canfield, M. Kauranen, Y. Svirko, and J. Turunen, Multipole Interference in the Second-Harmonic Optical Radiation from Gold Nanoparticles, Phys. Rev. Lett. **98**, 167403 (2007).

[4] M. Zdanowicz, S. Kujala, H. Husu, and M. Kauranen, Effective medium multipolar tensor analysis of second-harmonic generation from metal nanoparticles, New J. Phys. **13**, 023025 (2011).

[5] H. B. Aguiar, S. Gigan, and S. Brasselet, Polarization recovery through scattering media, Sci. Adv. **3**, e1600743 (2017).

[6] J. P. B. Mueller, N. A. Rubin, R. C. Devlin, B. Groever, and F. Capasso, Metasurface Polarization Optics: Independent Phase Control of Arbitrary Orthogonal States of Polarization, Phys. Rev. Lett. **118**, 113901 (2017).

[7] P. Genevet, F. Capasso, F. Aieta, M. Khorasaninejad, and R. Devlin, Recent advances in planar optics: from plasmonic to dielectric metasurfaces, Optica **4**, 139 (2017).

[8] Q. He, S. Sun, S. Xiao, and L. Zhou, High-efficiency metasurfaces: principles, realizations, and applications, Adv. Opt. Mater. **6**, 1800415 (2018).

[9] Q. Song, S. Khadir, S. Vézian, B. Damilano, P. D. Mierry, S. Chenot, V. Brandli, and P. Genevet, Bandwidth-unlimited polarization-maintaining metasurfaces, Sci. Adv. **7**, eabe1112 (2021).

[10] Y. Yuan, K. Zhang, B. Ratni, Q. Song, X. Ding, Q. Wu, S. N. Burokur, and P. Genevet, Independent phase modulation for quadruplex polarization channels enabled by chirality-assisted geometric-phase metasurfaces, Nat. Commun. **11**, 4186 (2020).

[11] Q. Song, S. Khadir, S. Vézian, B. Damilano, P. de Mierry, S. Chenot, V. Brandli, R. Laberdesque, B. Wattellier, and P. Genevet, Printing polarization and phase at the optical diffraction limit: near-and far-field optical encryption, Nanophotonics **10**, 697 (2021).

[12] G. Li, S. Zhang, and T. Zentgraf, Nonlinear photonic metasurfaces, Nat. Rev. Mater. **2**, 17010 (2017).

[13] A. Krasnok, M. Tymchenko, and A. Alù, Nonlinear metasurfaces: a paradigm shift in nonlinear optics, Mater. Today **21**, 8 (2018).

[14] B. Sain, C. Meier, and T. Zentgraf, Nonlinear optics in all-dielectric nanoantennas and metasurfaces: a review, Adv. Photon. **1**, 024002 (2019).

[15] J. Lee, M. Tymchenko, C. Argyropoulos, P. Chen, F. Lu, F. Demmerle, G. Boehm, M. Amann, A. Alù, and M. A. Belkin, Giant nonlinear response from plasmonic metasurfaces coupled to intersubband transitions, Nature (London) **511**, 65 (2014).

[16] D. Kim, H. Chung, J. Yu, I. Hwang, S. Park, F. Demmerle, G. Boehm, M. Amann, M. A. Belkin, J. Jung, and J. Lee, Spin-controlled nonlinear harmonic generations from plasmonic metasurfaces coupled to intersubband transitions, Adv. Opt. Mater. **8**, 2000004 (2020).

[17] T. Stolt, J. Kim, S. Héron, A. Vesala, Y. Yang, J. Mun, M. Kim, M. J. Huttunen, R. Czaplicki, M. Kauranen, J. Rho, and P. Genevet, Backward Phase-Matched Second-Harmonic Generation from Stacked Metasurfaces, Phys. Rev. Lett. **126**, 033901 (2021).

[18] L. Wang, S. Kruk, K. Koshelev, I. Kravchenko, B. Luther-Davies, and Y. Kivshar, Nonlinear wavefront control with all-dielectric metasurfaces, Nano Lett. **18**, 3978 (2018).

[19] B. Liu, B. Sain, B. Reineke, R. Zhao, C. Meier, L. Huang, Y. Jiang, and T. Zentgraf, Nonlinear wavefront control by geometric-phase dielectric metasurfaces: Influence of mode field and rotational symmetry, Adv. Opt. Mater. **8**, 1902050 (2020).

[20] C. Schlickriede, S. S. Kruk, L. Wang, B. Sain, Y. Kivshar, and T. Zentgraf, Nonlinear imaging with all-dielectric metasurfaces, Nano Lett. **20**, 4370 (2020).

[21] G. Li, G. Sartorello, S. Chen, L. H. Nicholls, K. F. Li, T. Zentgraf, S. Zhang, and A. V. Zayats, Spin and geometric phase control four-wave mixing from metasurfaces, Laser Photonics Rev. **12**, 1800034 (2018).

[22] Z. Lin, L. Huang, Z. T. Xu, X. Li, T. Zentgraf, and Y. Wang, Four-wave mixing holographic multiplexing based on nonlinear metasurfaces, Adv. Opt. Mater. **7**, 1900782 (2019).

[23] M. Tymchenko, J. S. Gomez-Diaz, J. Lee, N. Nookala, M. A. Belkin, and A. Alù, Gradient Nonlinear Pancharatnam-Berry Metasurfaces, Phys. Rev. Lett. **115**, 207403 (2015).

[24] N. Nookala, J. Lee, M. Tymchenko, J. S. Gomez-Diaz, F. Demmerle, G. Boehm, K. Lai, G. Shvets, M. Amann, A. Alù, and M. Belkin, Ultrathin gradient nonlinear metasurface with a giant nonlinear response, Optica **3**, 283 (2016).

[25] K. Chaudhuri, A. Shaltout, D. Shah, U. Guler, A. Dutta, V. M. Shalaev, and A. Boltasseva, Photonic spin Hall effect in robust phase gradient metasurfaces utilizing transition metal nitrides, ACS Photonics **6**, 99 (2019).

[26] Z. Gao, S. Golla, R. Sawant, V. Osipov, G. Briere, S. Vezian, B. Damilano, P. Genevet, and K. E. Dorfman, Revealing topological phase in Pancharatnam-Berry metasurfaces using mesoscopic electrodynamics, Nanophotonics **9**, 4711 (2020).

[27] J. Butet, G. Bachelier, I. Russier-Antoine, C. Jonin, E. Benichou, and P. F. Brevet, Interference between Selected Dipoles and Octupoles in the Optical Second-Harmonic Generation from Spherical Gold Nanoparticles, Phys. Rev. Lett. **105**, 077401 (2010).

[28] N. K. Balla, C. Rendon-Barraza, L. M. Hoang, P. Karpinski, E. Bermùdez-Ureña, and S. Brasselet, Polarized nonlinear nanoscopy of metal nanostructures, ACS Photonics **4**, 292 (2017).

[29] K. Koskinen, R. Czaplicki, A. Slablab, T. Ning, A. Hermans, B. Kuyken, V. Mittal, G. S. Murugan, T. Niemi, R. Baets, and M. Kauranen, Enhancement of bulk second-harmonic generation from silicon nitride films by material composition, Opt. Lett. **42**, 5030 (2017).

[30] Y. Gao, X. Xiong, Z. Wang, F. Chen, R. Peng, and M. Wang, Simultaneous Generation of Arbitrary Assembly of Polarization States with Geometrical-Scaling-Induced Phase Modulation, Phys. Rev. X **10**, 031035 (2020).

[31] Q. Song, A. Baroni, R. Sawant, P. Ni, V. Brandli, S. Chenot, S. Vézian, B. Damilano, P. Mierry, S. Khadir, P. Ferrand, and P. Genevet, Ptychography retrieval of fully polarized holograms from geometric-phase metasurfaces, Nat. Commun. **11**, 2651 (2020).

[32] X. Zhang, Q. Li, F. Liu, M. Qiu, S. Sun, Q. He, and L. Zhou, Controlling angular dispersions in optical metasurfaces, Light: Sci. Appl. **9**, 76 (2020).

[33] J. W. Chen, K. Wang, H. Long, X. Han, H. Hu, W. Liu, B. Wang, and P. Lu, Tungsten disulfide-gold nanohole hybrid metasurfaces for nonlinear metalenses in the visible region, Nano Lett. **18**, 1344 (2018).

[34] G. Hu, X. Hong, K. Wang, J. Wu, H. Xu, W. Zhao, W. Liu, S. Zhang, F. Garcia-Vidal, B. Wang, P. Lu, and C. Qiu, Coherent steering of nonlinear chiral valley photons with a synthetic Au-WS_2 metasurface, Nat. Photonics **13**, 467 (2019).

[35] S. Mukamel, *Principles of Nonlinear Optical Spectroscopy* (Oxford University Press, New York, 1995).

[36] K. E. Dorfman, P. K. Jha, D. V. Voronine, P. Genevet, F. Capasso, and M. O. Scully, Quantum-Coherence-Enhanced

Surface Plasmon Amplification by Stimulated Emission of Radiation, Phys. Rev. Lett. **111**, 043601 (2013).

[37] N. Bloembergen, *Nonlinear Optics* (Benjamin, New York, 1965).

[38] L. D. Landau and E. M. Lifshitz, *Electrodynamics of Continuous Media*, 2nd ed. (Pergamon, Amsterdam, 1984).

[39] J. Zuloaga, E. Prodan, and P. Nordlander, Quantum plasmonics: optical properties and tunability of metallic nanorods, ACS Nano **4**, 5269 (2010).

[40] H. Chen, L. Shao, Q. Lia, and J. Wang, Gold nanorods and their plasmonic properties, Chem. Soc. Rev. **42**, 2679 (2013).

[41] G. D. Valle, B. Hopkins, L. Ganzer, T. Stoll, M. Rahmani, S. Longhi, Y. S. Kivshar, C. D. Angelis, D. N. Neshev, and G. Cerullo, Nonlinear anisotropic dielectric metasurfaces for ultrafast nanophotonics, ACS Photonics **4**, 2129 (2017).

[42] W. Liu, Z. Li, H. Cheng, S. Chen, and J. Tian, Momentum Analysis for Metasurfaces, Phys. Rev. Appl. **8**, 014012 (2017).

[43] M. Tymchenko, J. S. Gomez-Diaz, J. Lee, N. Nookala, M. A. Belkin, and A. Alù, Advanced control of nonlinear beams with Pancharatnam-Berry metasurfaces, Phys. Rev. B **94**, 214303 (2016).

[44] S. D. Gennaro, Y. Li, S. A. Maier, and R. F. Oulton, Nonlinear Pancharatnam-Berry phase metasurfaces beyond the dipole approximation, ACS Photonics **6**, 2335 (2019).

[45] J. Zhang, X. Zhao, Y. Zheng, and X. Chen, Generalized nonlinear Snell's law at $\chi^{(2)}$ modulated nonlinear metasurfaces: anomalous nonlinear refraction and reflection, Opt. Lett. **44**, 431 (2019).

[46] L. Huang, S. Zhang, and T. Zentgraf, Metasurface holography: from fundamentals to applications, Nanophotonics **7**, 1169 (2018).

[47] L. Zhang, X. Chen, S. Liu, Q. Zhang, J. Zhao, J. Y. Dai, G. D. Bai, X. Wan, Q. Cheng, G. Castaldi, V. Galdi, and T. J. Cui, Space-time-coding digital metasurfaces, Nat. Commun. **9**, 4334 (2018).

[48] T. Stav, A. Faerman, E. Maguid, D. Oren, V. Kleiner, E. Hasman, and M. Segev, Quantum entanglement of the spin and orbital angular momentum of photons using metamaterials, Science **361**, 1101 (2018).

[49] P. Georgi, M. Massaro, K. Luo, B. Sain, N. Montaut, H. Herrmann, T. Weiss, G. Li, C. Silberhorn, and T. Zentgraf, Metasurface interferometry toward quantum sensors, Light: Sci. Appl. **8**, 70 (2019).

[50] L. Li, Z. Liu, X. Ren, S. Wang, V. Su, M. Chen, C. H. Chu, H. Y. Kuo, B. Liu, W. Zang, G. Guo, L. Zhang, Z. Wang, S. Zhu, and D. P. Tsai, Metalens-array-based high-dimensional and multiphoton quantum source, Science **368**, 1487 (2020).